Waitman Filho, S., & Marcos, A. (2019). Active flutter suppression: non-structured and structured H design. *IFAC-PapersOnLine*, *52*(12), 146-151. https://doi.org/10.1016/j.ifacol.2019.11.184

Active flutter suppression: non-structured and structured H_∞ design ⋆

Sérgio Waitman * **Andrés Marcos** *

* *Aerospace Engineering Department, University of Bristol, University Walk, Bristol, UK BS8 1TR (e-mail: {sergio.waitman, andres.marcos}@bristol.ac.uk).*

Abstract: In this article a comparison of two controllers for the active suppression of flutter of a flexible remotely-piloted aerial vehicle is presented. The H_∞ technique is used for both, but the first relies on the standard (non-structured) approach and the second on the structured synthesis. High-fidelity models derived from finite element modeling are used to verify the performance of the obtained controllers. Reduced-order models are used for the control synthesis, which are obtained from applying a combination of balanced and modal reduction techniques on the high-fidelity models. The results show that both controllers are similar in performance and robustness, and both are capable of suppressing flutter and extending the flight envelope well beyond the open-loop flutter speed.

Keywords: Aerospace, aircraft control, H_∞ control, robust control

1. INTRODUCTION

Aeroelastic flutter is the phenomenon that takes place when there is a positive feedback caused by the coupling between the aerodynamic loads of a structure in a fluid flow with its natural modes of vibration. The result is an unstable oscillatory motion that, if not controlled, may lead to structural failure (Hodges and Pierce, 2011). Due to its catastrophic consequences, flutter is critical for aircraft design, and thus conventional aircraft are designed such that flutter does not occur within their operational flight envelope. This is normally achieved via the addition of structural mass to increase stiffness, at the expense of energetic efficiency, and safety margins on the envelope, at the expense of performance capability.

An alternative approach to the above passive remedies is to include an active flutter suppression (AFS) system. With this technique, the control surfaces of the aircraft are used to counteract the positive feedback effect of flutter, thus increasing the damping and reducing the oscillation of the wings. AFS may reduce the need for structural stiffening masses, which could lead to aircraft with improved performance and energy efficiency.

The EU's Horizon 2020 project *Flutter Free Flight Envelope eXpansion for ecOnomical Performance improvement* (FLEXOP) was conceived to tackle these issues. The project is devoted to developing multidisciplinary aircraft design capabilities by achieving a closer coupling of wing aeroelasticity and flight control systems in the design phase. The main goal is to increase the Technology Readiness Level (TRL) of aeroelastic aircraft design, including passive (Sodja et al., 2019) and active (Luspay et al., 2019) flutter suppression techniques. This will be achieved via flight-test validation using a flexible-wing remotely-piloted demonstrator, currently being built by the FLEXOP consortium (Meddaikar et al., 2019; Roëßler et al., 2019).

A comprehensive historical review on AFS techniques is provided by Livne (2018). Early approaches were based on the knowledge of the physical and mathematical aspects of the flutter mechanism. Among such techniques, one could mention *Identically Located Actuators and Forces* (ILAF) (Wykes, 1968), which exploits the advantages resulting from adequately positioning actuators and sensors in the wing. With the parallel development of advanced control design techniques and computational capabilities, attention has been shifted to more general control-theory techniques, such as Linear Quadratic Gaussian (LQG) (Gangsaas and Ly., 1979) and H_∞ control (Theis et al., 2016). Even though much work has been done, Livne (2018) identifies control law design as one of the major points to be addressed in future research on AFS to advance the state of the art and the TRL.

This paper describes the design of H_∞ controllers to provide AFS for the FLEXOP demonstrator. The standard (i.e. non-structured) H_∞ approach was chosen due to its ability to systematically address constraints in the frequency domain, such as restraining control action to a given frequency range and providing damping to the flutter modes. H_∞ control has the disadvantage that the obtained controller can be of high order, which can hinder its implementation in the Flight Control Computer (FCC) when limited computational resources are available (as in the case of UAVs). For this reason, a model reduction may be needed before the controller can be used, but this reduction can lead to unacceptable performance degradation. To cope with this issue, a second design is performed using the structured H_∞ control approach (Apkarian and Noll, 2006; Gahinet and Apkarian, 2011). This technique

⋆ This project has received funding from the European Union's Horizon 2020 research and innovation programme under grant agreement No 636307.

uses non-smooth optimization tools to synthesize a controller minimizing an H_∞ metric, and allows for the consideration of additional structural constraints on the controller such as fixed order or fixed structure. Another advantage of this approach is the possibility to synthesize multi-plant and/or auto-scheduled controllers. Although the underlying problem is non-convex and NP-hard, the optimization procedure is shown to always converge to a local minimum (Apkarian and Noll, 2006). Moreover, it has been shown to yield promising results in a wide range of applications, including space missions and aircraft control (Marcos and Sato, 2017).

The FLEXOP demonstrator is described in Section 2, together with the models of the aircraft and of its actuators and sensors. Section 3 is devoted to the design of controllers for active flutter suppression using both the traditional H_∞ loop shaping and the structured H_∞ techniques. The performance provided by both controllers is analyzed in Section 4 using time and frequency analyses.

2. AIRCRAFT MODEL

The FLEXOP demonstrator is a remotely-piloted flexible aircraft with a wing span of 7 m and a maximum takeoff weight of around 65 kg. It was designed such that flutter occurs at an airspeed below 55 m/s, with a first-mode flutter frequency below 10 Hz (Stahl et al., 2017). Each wing of the UAV is equipped with four control surfaces, with the outermost flaps reserved for flutter control. A direct drive mechanism is used to ensure that a large actuation bandwidth is available for active flutter suppression. A schematic of the aircraft with its actuators is shown in Fig. 1. A set of 6 inertial measurement units (IMUs) is installed in each wing to provide measurements for the flutter controller, shown in Fig. 2.

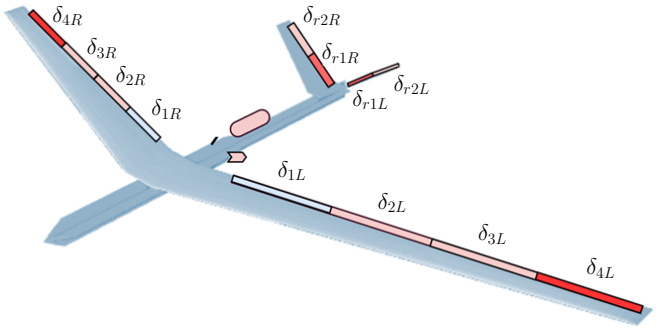

Fig. 1. Actuators of the FLEXOP demonstrator.

A fully-flexible nonlinear model of the UAV has been developed using the double lattice method coupled with a finite elements model of the structural dynamics (Wuestenhagen et al., 2018). This high-fidelity model contains 1152 states describing the rigid-body motion and the aeroelastic dynamics. It was trimmed and linearized around 26 cruise level flight conditions with true airspeed ranging from $V_{\mathrm{TAS}} = 45$ up to 70 m/s. From this family of high-fidelity (HF) state-space models, a combination of balanced and modal reduction techniques (Skogestad and Postlethwaite, 2001) was applied to obtain a set of 40-state reduced-order models (ROM) for flutter control design. The pole map of

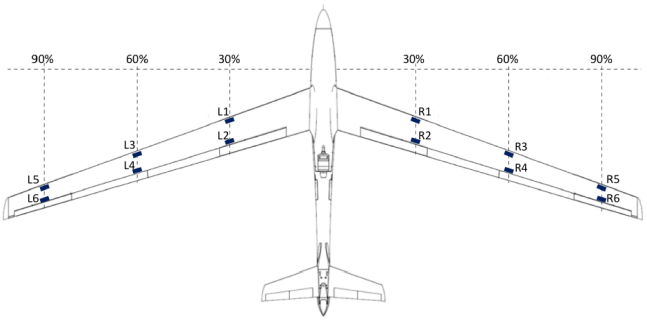

Fig. 2. Sensors of the FLEXOP demonstrator.

the full- and reduced-order controllers in terms of the true airspeed V_{TAS} is shown in Fig. 3 in next page. The inset focus on the poles associated with the first symmetric and antisymmetric flutter modes, denoted respectively by η_1 and η_2. It shows that the reduced-order models provide an adequate approximation of the flutter dynamics. The two pair of complex conjugate poles approach the imaginary axis with increasing airspeed, until instability is reached at 52 m/s – termed the open-loop flutter speed.

The parasitic dynamics introduced by the measurement-actuation chain are considered next. A model of the direct drive actuator was identified as a fourth-order transfer function given by (Luspay et al., 2019):

$$G_{\mathrm{act}}(s) = \frac{(2.741{\cdot}10^5 s^2 + 3.117{\cdot}10^6 s + 1.024{\cdot}10^8)e^{-0.0001s}}{s^4 + 575.8s^3 + 2.814{\cdot}10^5 s^2 + 3.324{\cdot}10^6 s + 1.025{\cdot}10^8}. \tag{1}$$

The IMUs have a bandwidth of 200 Hz, and are modeled as first-order systems:

$$G_{\mathrm{IMU}}(s) = \frac{2\pi 200}{s + 2\pi 200}. \tag{2}$$

Finally, the delay from the FCC is estimated to be around 10 ms, and is modeled as a pure delay $G_{\mathrm{delay}}(s) = e^{-0.01s}$ acting on the controller output.

3. ROBUST CONTROLLER DESIGN

The aim of the controller design is to extend the flight envelope by increasing the closed-loop flutter speed. To deal with both symmetric and antisymmetric flutter modes, the measurements used by the flutter controller are also split into symmetric and antisymmetric channels ($a_{z,\mathrm{S}}$ and $a_{z,\mathrm{AS}}$) according to

$$\begin{bmatrix} a_{z,\mathrm{S}} \\ a_{z,\mathrm{AS}} \end{bmatrix} = \begin{bmatrix} \frac{1}{2} & \frac{1}{2} & -1 \\ \frac{1}{2} & -\frac{1}{2} & 0 \end{bmatrix} \begin{bmatrix} a_{z,\mathrm{wL}} \\ a_{z,\mathrm{wR}} \\ a_{z,\mathrm{cg}} \end{bmatrix}, \tag{3}$$

where $a_{z,\mathrm{wL}}$ and $a_{z,\mathrm{wR}}$ represent the mean of the z-axis acceleration measurements provided respectively by the left and right pair of wingtip IMUs (sensors L/R5 and L/R6 in Fig. 2), and $a_{z,\mathrm{cg}}$ is the z-axis acceleration at the center of gravity. The latter is subtracted in the symmetric channel to provide a decoupling between the flutter measurements and the rigid-body dynamics of the aircraft (Jeanneau et al., 2004). In the same vein, the control action is split into symmetric and antisymmetric channels δ_{S} and δ_{AS}, which are allocated to the flutter control surfaces according to

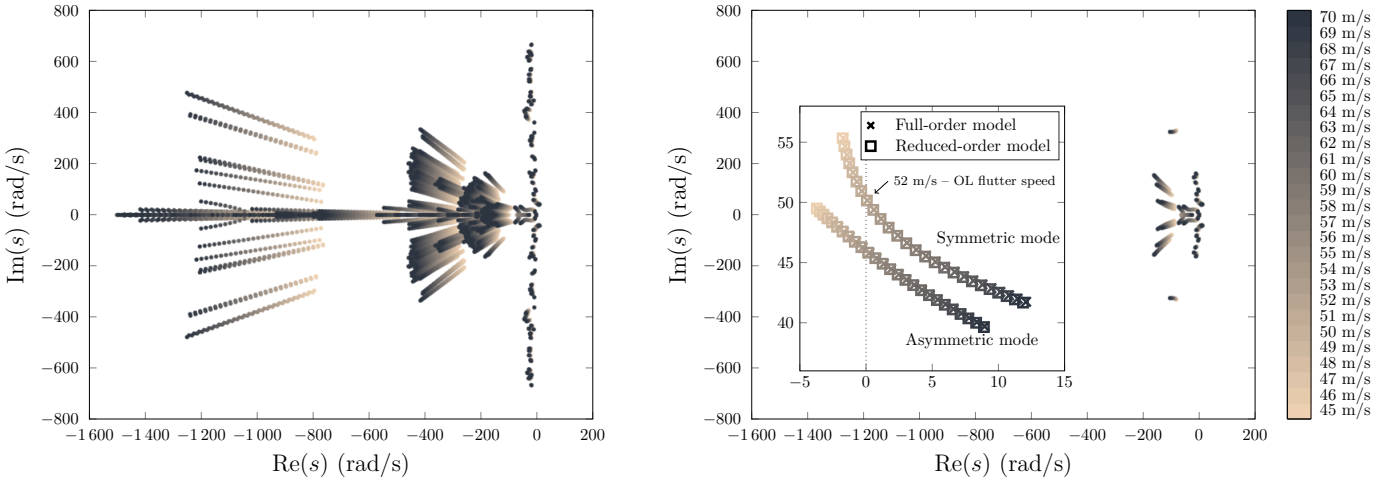

Fig. 3. Pole map of full- (left) and reduced-order (right) models.

$$\begin{bmatrix} \delta_{4\mathrm{L}} \\ \delta_{4\mathrm{R}} \end{bmatrix} = \begin{bmatrix} \frac{1}{2} & \frac{1}{2} \\ \frac{1}{2} & -\frac{1}{2} \end{bmatrix} \begin{bmatrix} \delta_{\mathrm{S}} \\ \delta_{\mathrm{AS}} \end{bmatrix}. \tag{4}$$

In the standard H_∞ control, the controller has the same number of states as the generalized plant (systems and design weights). In order to reduced the dimension of the synthesis model, the measurement-actuation chain dynamics are reduced. First, since the same linear model G_{IMU} is used for all measurement channels, it is shifted to the input of the system. The parasitic dynamics chain is then given by $G_{\mathrm{chain}} := G_{\mathrm{act}} G_{\mathrm{IMU}} G_{\mathrm{delay}}$. A fifth-order Padé approximation $G_{\mathrm{Padé}}$ is computed from G_{chain}, and is subsequently reduced by balanced residualization to obtain a third-order reduced model G_{red}. The reduced model accurately represents the phase loss due to the parasitic dynamics around the flutter eigenfrequencies.

The goal of the control design is achieved by damping the flutter modes around the open-loop flutter speed. In order to take this into account in the H_∞ criterion, the generalized modal velocities of the first symmetric and antisymmetric flutter modes, $\dot{\eta}_1$ and $\dot{\eta}_2$, are considered as performance outputs. In this way, the damping of the flutter modes is directly seen as the amplitude of the peaks in the transfer function between the actuators $(a_{z,\mathrm{S}}, a_{z,\mathrm{AS}})$ and the performance channels $(\dot{\eta}_1, \dot{\eta}_2)$.

In view of the goal to extend the flight envelope, the controllers are designed using the reduced-order models at $V_{\mathrm{TAS}} = 59$ m/s, denoted $G_{\mathrm{r},59}$, i.e. above the open-loop flutter speed. The overall synthesis model G_{syn} is shown in Fig. 4.

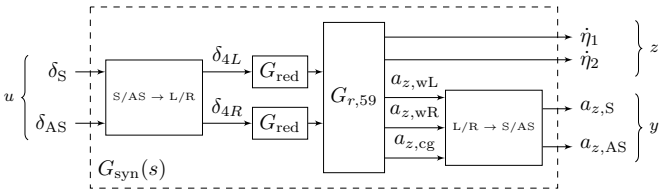

Fig. 4. Synthesis model for H_∞ control design.

3.1 Coupled standard H_∞ controller

This section describes the design of the (non-structured) H_∞ AFS controller. The performance specifications are translated into a weighted H_∞ criterion via the addition of weighting functions to obtain the generalized plant represented in Fig. 5. Five weights are added, namely W_d, W_n, W_y, W_z and W_u, and the design rationale uses a coupled approach in terms of the simultaneous tackling of symmetric and antisymmetric modes.

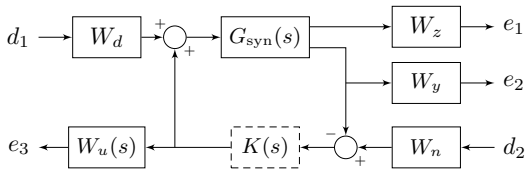

Fig. 5. Generalized plant for H_∞ design.

The weight W_u is used to shape the controller transfer function and confine the control action around the flutter eigenfrequencies, thus avoiding interaction with the low-frequency rigid-body dynamics and the high-frequency flexible modes. The same band-stop transfer function is then chosen for the symmetric and antisymmetric channels, given by

$$\tilde{W}_u(s) = 40 \frac{s^2 + 101s + 2200}{s^2 + 127020s + 2200}. \tag{5}$$

The desired damping for the flutter modes is imposed via the weight W_z, whose values are chosen to bound the peaks of the transfer function of G_{syn} between the actuators and the performance channels. The weight W_d is fixed as the identity matrix, to serve as a normalization reference for the other weights, and W_n and W_y are chosen to normalize the input-output of the plant, i.e. to obtain a transfer function with gain close to unity on all channels. After tuning, the chosen weighting functions are given by

$$\begin{aligned} W_d &= I_2 & W_z &= 0.01\,\mathrm{diag}(5, 6) \\ W_n &= 150 I_2 & W_y &= 0.001\,\mathrm{diag}(1.7, 1.7) \\ & & W_u(s) &= \mathrm{diag}\left(\tilde{W}_u(s), \tilde{W}_u(s)\right). \end{aligned} \tag{6}$$

The controller is designed by solving a standard H_∞ problem, i.e. by finding the controller K that minimizes the H_∞ gain from (d_1, d_2) to (e_1, e_2, e_3) in Fig. 5. This is done numerically in Matlab® using the command `hinfsyn`. The optimum controller yields a closed-loop H_∞ gain of $\gamma_* = 0.9923$. To improve the numerical conditioning of the controller, a sub-optimal solution is subsequently obtained that ensures an H_∞ gain of $\gamma = 1.0799$. This is still sufficiently close to 1, meaning that the performance specifications have been satisfied by the closed-loop system.

As discussed earlier, the (full-order) H_∞ controller K has the same number of states as the model used for the design. The generalized plant has 50 states, 40 coming from G_{syn} plus 4 from W_u and 3 from each G_{red}. Since the controller must run in real time in the flight control computer, it should not require extensive computation so as not to overburden the computing power of the processor. For this reason, the controller is reduced using balanced truncation to obtain a better approximation in the frequency domain. To ensure appropriate roll-off of the controller, the D matrix of the reduced-order controller K_r is set to 0. The number of states is chosen to limit the performance degradation caused by the model reduction. In this way, a 15-state K_r is obtained, which ensures a closed-loop H_∞ gain of $\gamma_r = 1.0801$, i.e. 0.0175% above that for the full-order controller. The frequency response of both controllers is shown in Fig. 6.

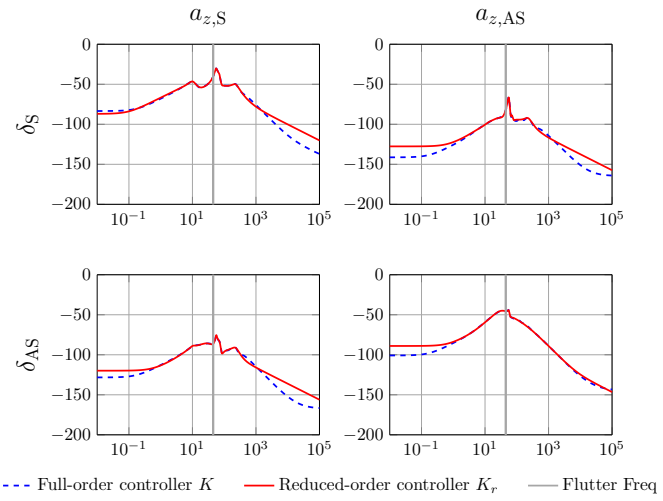

Fig. 6. Bode plots of K and K_r.

3.2 Decoupled structured H_∞ controller

The structured H_∞ synthesis technique allows to fix a priori the order or architecture (e.g. PID, state feedback...) of the controller. In this work, this is exploited to capitalize on the decoupling between the symmetric and antisymmetric channels of the controller. Indeed, as seen in Fig. 6, the reduced controller K_r designed in Section 3.1 has a difference of 40 dB between the direct channels ($a_{z,\text{S}} \to \delta_\text{S}$ and $a_{z,\text{AS}} \to \delta_\text{AS}$) and the cross-coupling terms ($a_{z,\text{S}} \to \delta_\text{AS}$ and $a_{z,\text{AS}} \to \delta_\text{S}$). This suggests that the control actions in the symmetric and antisymmetric channels are essentially decoupled. For this reason, a decoupled structure with two SISO controllers is adopted for the design of the structured controller K_s, see Fig. 7.

The design of the decoupled controller is done using the same generalized plant (Fig. 5) and weights (Eq. (6)) as in the previous section. Being a non-convex optimization problem, the design of structured H_∞ controllers is dependent on the choice of appropriate initial conditions. For this reason, the previous (non-structured) reduced-order H_∞ controller K_r is used as a basis for the new design. As decoupled controller versions, $K_{\text{r,S}}$ and $K_{\text{r,AS}}$, are required, a series of balanced residualizations are performed on K_r. For the symmetric controller, $K_{\text{r,S}}$, the symmetric channel of K_r is residualized sequentially with decreasing dimension. When degradation was spotted between the frequency responses of $K_{\text{r,S}}$ and of the symmetric channel for K_r, the procedure was stopped, and the previous value selected, obtaining finally a $K_{\text{r,S}}$ with 9 states. Using the same methodology, a 6-state controller $K_{\text{r,AS}}$ is also obtained, so that K_s will have 15 states. In addition, 150 randomly generated points are also used as initial conditions. Since the structured H_∞ optimization problem is non-convex, this is important to minimize the chances of getting stuck in a local minimum far from the optimum.

As in the last section, the D matrix of the controllers is set to 0 to enforce sufficient roll-off of the controllers in the high-frequency range. The matrices A, B and C of the symmetric and antisymmetric parts of the structured controller are fully tunable, so that the optimization problem has 147 free parameters (99 from the 9-state $K_{\text{r,S}}$ and 48 from the 6-state $K_{\text{r,AS}}$).

The controller is synthesized numerically in Matlab® via the routine `hinfstruct`. The results of the optimization are shown in Fig. 8, in ascending order of γ. The optimization run starting from K_r (in blue) shows the best performance among all the initial conditions. The gray bars represent the optimization runs that were able to converge to a stable closed-loop system, while the red ones represent the cases where the closed loop was unstable. This set of solutions of the structured H_∞ optimization problem shows how sensitive it can be with respect to the initial condition. It also illustrates how having a physically meaningful starting controller can help the solver to attain better results. In this case, the obtained H_∞ gain was of $\gamma_s = 0.9994$, which is only 0.6520% above the optimal H_∞ controller designed in Section 3.1.

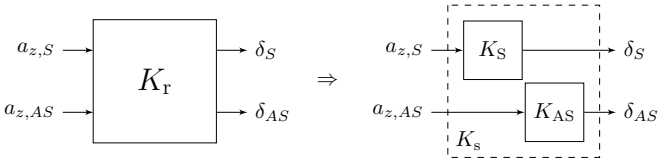

Fig. 7. Decoupled structured controller.

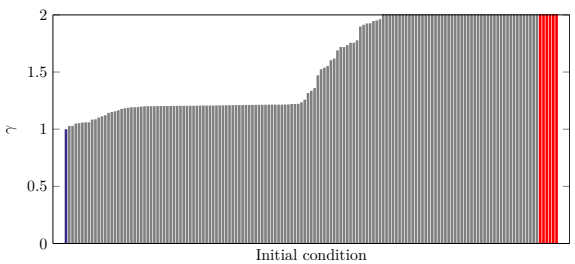

Fig. 8. Obtained γ in structured H_∞ design.

Fig. 9 shows the frequency responses of the (15-state) K_r and K_s controllers. The decoupling structure of K_s is indicated by the absence of transfer functions for $a_{z,\mathrm{S}} \to \delta_\mathrm{AS}$ and $a_{z,\mathrm{AS}} \to \delta_\mathrm{S}$. The controllers are very similar around the flutter eigenfrequencies, with K_s presenting slightly higher amplitudes in the low- and high-frequency ranges.

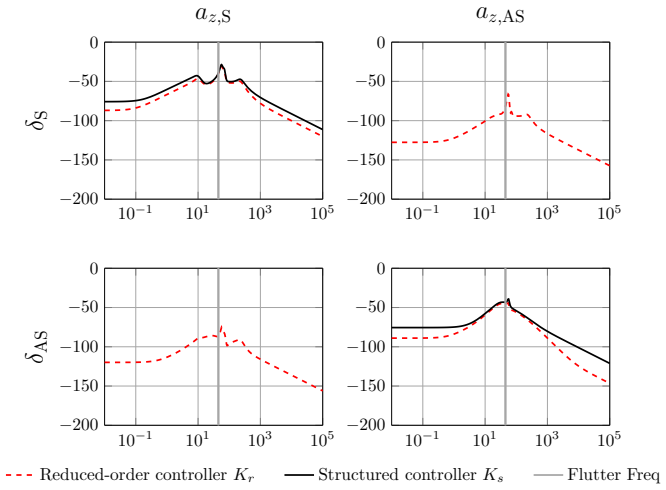

Fig. 9. Bode plots of K_r and K_s

A comparison between the poles of K_r and K_s is given in Fig. 10, with a zoom on the inset. The similarity between the poles of both controllers, together with the fact that K_s yielded a closed-loop gain close to the non-structured optimum, suggests that the reduction from K to K_r did not affect much the controller's performance, thus leaving little margin for improvement with the structured approach. This is further confirmed by the 0.0175% performance degradation loss from K to K_r.

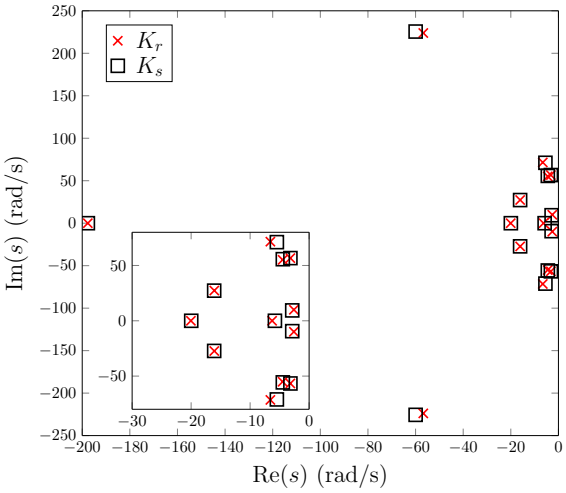

Fig. 10. Pole map of K_r and K_s.

4. CLOSED-LOOP ANALYSIS

The analysis of the closed loops using K_r and K_s is performed using the 1152-state HF linearized models. Using $G_\mathrm{Padé}$ as an approximation of the parasitic dynamics, the pole map of the closed-loop system for K_r is shown in Figure 11. The red square marks represent the open-loop flutter modes, for comparison, while the circles denote the open- and closed-loop poles at the design speed (59 m/s). The pole map for K_s is very similar. Both controllers provide damping to the flutter modes and extend the flight envelope to attain a closed-loop flutter speed of 63 m/s, an increase of around 21% with respect to the open loop.

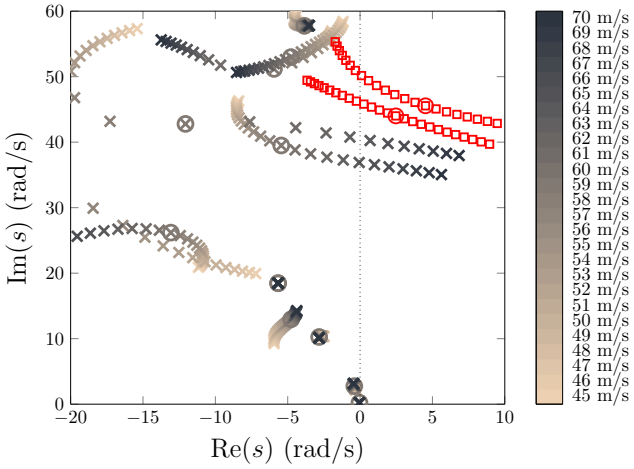

Fig. 11. Closed-loop pole map with K_r.

The maximum singular value (σ) plot from the flutter control surfaces $(\delta_\mathrm{S}, \delta_\mathrm{AS})$ to the generalized modal velocities of the flutter modes $(\dot{\eta}_1, \dot{\eta}_2)$ of K_s is shown in Figure 12 for speeds ranging from 45 up to 61 m/s. The plot clearly shows that the peaks associated with the flutter modes are effectively damped in closed-loop in this whole speed range. Although the plots for both controllers are similar, K_s provides a little more damping at higher speeds while having a slightly higher impact at higher frequencies.

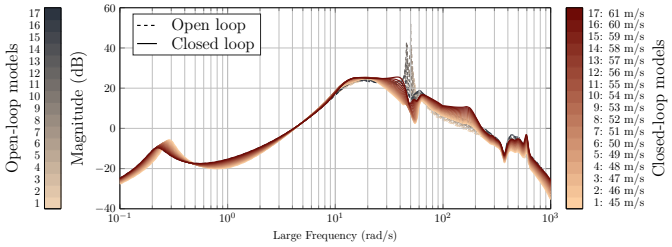

Fig. 12. Maximum σ from $(\delta_\mathrm{S}, \delta_\mathrm{AS})$ to $(\dot{\eta}_1, \dot{\eta}_2)$ with K_s.

For the closed-loop time-domain analysis, the plant is augmented with an elevator input and rigid-body motion measurements. Fig. 13 shows the response of the open- (blue dashed line) and closed-loop systems for both controllers (red solid for K_r and black dash-dot for K_s) to a step input in the elevator at the open-loop flutter speed (52 m/s). Both controllers damp the flutter-induced oscillations using little control action and in less than 1 second. It can also be seen (from the pitch rate and vertical acceleration at c.g.) that the controllers do not affect the rigid-body motion of the aircraft. This is important to minimize the coupling between the flutter controller and the auto-pilot. The structured controller K_s shows better decoupling in the antisymmetric channel, as seen by the increased damping of the oscillations in $a_{z,\mathrm{AS}}$ and by the reduced control action in δ_AS.

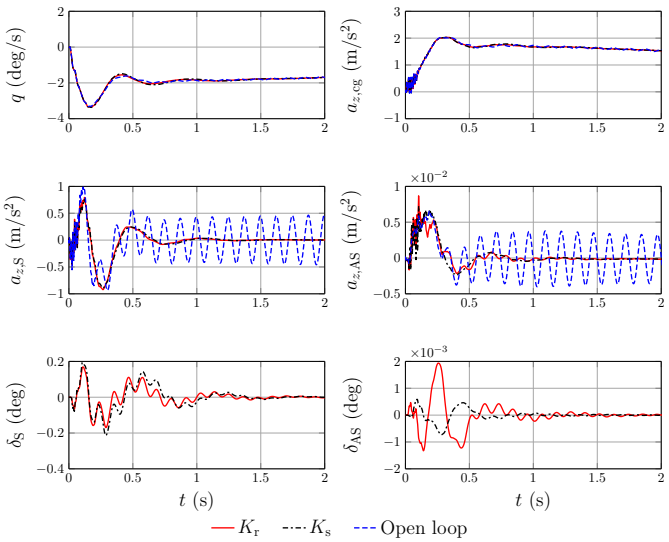

Fig. 13. Elevator step response at 52 m/s.

5. CONCLUSION

This paper presented the design of standard H_∞ and structured H_∞ controllers for active flutter suppression of a flexible flying demonstrator. Based on the symmetric and antisymmetric nature of the flutter dynamics, the controllers are designed using measurements as well as controls of the symmetric and antisymmetric motion of the wing. Further exploration of this separation led to the design of an explicitly decoupled structured H_∞ controller. Comparison between both controllers in time and frequency domains showed that they perform similarly, yet K_s provides better decoupling as expected. Ongoing research is focused on further extension of the flight envelope using gain scheduling and linear parameter varying techniques. Flight tests of the flexible aircraft are scheduled for spring/summer 2019 for validation of the flutter suppression capabilities of the controllers developed within the FLEXOP project.

REFERENCES

Apkarian, P. and Noll, D. (2006). Nonsmooth H_∞ synthesis. *IEEE Transactions on Automatic Control*, 51(1), 71–86. doi:10.1109/TAC.2005.860290.

Gahinet, P. and Apkarian, P. (2011). Structured H_∞ synthesis in MATLAB. *IFAC Proceedings Volumes*, 44(1), 1435–1440. doi:10.3182/20110828-6-IT-1002.00708. 18th IFAC World Congress.

Gangsaas, D. and Ly., U.L. (1979). Application of a modified linear quadratic gaussian design to active control of a transport airplane. In *Guidance, Navigation, and Control and Co-located Conferences*. American Institute of Aeronautics and Astronautics. doi:10.2514/6.1979-1746.

Hodges, D.H. and Pierce, G.A. (2011). *Introduction to Structural Dynamics and Aeroelasticity*. Cambridge University Press, second edition.

Jeanneau, M., Aversa, N., Delannoy, S., and Hockenhull, M. (2004). AWIATOR's study of a wing load control: Design and flight-test results. In *IFAC Symposium on Automatic Control in Aerospace*, volume 37, 469–474. doi:10.1016/S1474-6670(17)32219-X.

Livne, E. (2018). Aircraft active flutter suppression: State of the art and technology maturation needs. *Journal of Aircraft*, 55(1), 410–452. doi:10.2514/1.c034442.

Luspay, T., Baár, T., Teubl, D., Vanek, B., Ossmann, D., Wüstenhagen, M., Pusch, M., Kier, T.M., Waitman, S., Iannelli, A., Marcos, A., and Lowenberg, M.H. (2019). Flight control design for a highly flexible flutter demonstrator. In *AIAA SciTech Forum*. American Institute of Aeronautics and Astronautics. doi:10.2514/6.2019-1817.

Marcos, A. and Sato, M. (2017). Flight testing of an structured H-infinity controller: An EU-Japan collaborative experience. In *IEEE Conference on Control Technology and Applications (CCTA)*, 2132–2137. doi:10.1109/CCTA.2017.8062768.

Meddaikar, Y.M., Dillinger, J., Klimmek, T., Krüger, W., Wüstenhagen, M., Kier, T.M., Hermanutz, A., Hornung, M., Rozov, V., Breitsamter, C., Alderman, J., Takarics, B., and Vanek, B. (2019). Aircraft aeroservoelastic modelling of the FLEXOP unmanned flying demonstrator. In *AIAA SciTech Forum*. American Institute of Aeronautics and Astronautics. doi:10.2514/6.2019-1815.

Roeßler, C., Stahl, P., Sendner, F., Hermanutz, A., Koeberle, S., Bartasevicius, J., Rozov, V., Breitsamter, C., Hornung, M., Meddaikar, Y.M., Dillinger, J., Sodja, J., De Breuker, R., Koimtzoglou, C., Kotinis, D., and Georgopoulos, P. (2019). Aircraft design and testing of FLEXOP unmanned flying demonstrator to test load alleviation and flutter suppression of high aspect ratio flexible wings. In *AIAA SciTech Forum*. American Institute of Aeronautics and Astronautics. doi:10.2514/6.2019-1813.

Skogestad, S. and Postlethwaite, I. (2001). *Multivariable Feedback Control: Analysis and Design*. John Wiley & Sons, second edition.

Sodja, J., Werter, N., and De Breuker, R. (2019). Design of a flying demonstrator wing for manoeuvre load alleviation with cruise shape constraint. In *AIAA SciTech Forum*. American Institute of Aeronautics and Astronautics. doi:10.2514/6.2018-2153.

Stahl, P., Sendner, F.M., Hermanutz, A., Rößler, C., and Hornung, M. (2017). Mission and aircraft design of FLEXOP unmanned flying demonstrator to test flutter suppression within visual line of sight. In *AIAA AVIATION Forum*, 3766. doi:10.2514/6.2017-3766.

Theis, J., Pfifer, H., and Seiler, P.J. (2016). Robust control design for active flutter suppression. In *AIAA SciTech Forum*. American Institute of Aeronautics and Astronautics. doi:10.2514/6.2016-1751.

Wuestenhagen, M., Kier, T., Meddaikar, Y.M., Pusch, M., Ossmann, D., and Hermanutz, A. (2018). Aeroservoelastic modeling and analysis of a highly flexible flutter demonstrator. In *2018 Atmospheric Flight Mechanics Conference*. American Institute of Aeronautics and Astronautics. doi:10.2514/6.2018-3150.

Wykes, J. (1968). Structural dynamic stability augmentation and gust alleviation of flexible aircraft. In *5th Annual Meeting and Technical Display*. American Institute of Aeronautics and Astronautics. doi:10.2514/6.1968-1067.